JGR Earth Surface

RESEARCH ARTICLE
10.1029/2018JF004823

Heat and Salt Flow in Subsea Permafrost Modeled with CryoGRID2

Michael Angelopoulos[1,2], Sebastian Westermann[3], Paul Overduin[1], Alexey Faguet[4,5], Vladimir Olenchenko[4,5], Guido Grosse[1,2], and Mikhail N. Grigoriev[6]

[1]Alfred Wegener Institute, Helmholtz Centre for Polar and Marine Research, Potsdam, Germany, [2]Institute of Geosciences, University of Potsdam, Potsdam, Germany, [3]Department of Geosciences, University of Oslo, Oslo, Norway, [4]Institute of Petroleum Geology and Geophysics, Russian Academy of Sciences, Novosibirsk, Russia, [5]Department of Geophysics, Novosibirsk State University, Novosibirsk, Russia, [6]Melnikov Permafrost Institute, Siberian Branch, Russian Academy of Sciences, Yakutsk, Russia

Key Points:
- The thawing of ice-bearing subsea permafrost was modeled by coupling heat and salt diffusion
- The boundary conditions reflect sea ice dynamics during the transition from terrestrial to marine permafrost
- The modeled ice-bearing permafrost depths were validated with geoelectric surveys

Correspondence to:
M. Angelopoulos,
michael.angelopoulos@awi.de

Citation:
Angelopoulos, M., Westermann, S., Overduin, P. P., Faguet, A., Olenchenko, V., Grosse, G., & Grigoriev, M. N. (2019). Heat and salt flow in subsea permafrost modeled with CryoGRID2. *Journal of Geophysical Research: Earth Surface*, *124*, 920–937. https://doi.org/10.1029/2018JF004823

Received 20 JUL 2018
Accepted 28 JAN 2019
Accepted article online 10 FEB 2019
Published online 6 APR 2019

The copyright line for this article was changed on 11 APR 2019 after original online publication.

Abstract Thawing of subsea permafrost can impact offshore infrastructure, affect coastal erosion, and release permafrost organic matter. Thawing is usually modeled as the result of heat transfer, although salt diffusion may play an important role in marine settings. To better quantify nearshore subsea permafrost thawing, we applied the CryoGRID2 heat diffusion model and coupled it to a salt diffusion model. We simulated coastline retreat and subsea permafrost evolution as it develops through successive stages of a thawing sequence at the Bykovsky Peninsula, Siberia. Sensitivity analyses for seawater salinity were performed to compare the results for the Bykovsky Peninsula with those of typical Arctic seawater. For the Bykovsky Peninsula, the modeled ice-bearing permafrost table (IBPT) for ice-rich sand and an erosion rate of 0.25 m/year was 16.7 m below the seabed 350 m offshore. The model outputs were compared to the IBPT depth estimated from coastline retreat and electrical resistivity surveys perpendicular to and crossing the shoreline of the Bykovsky Peninsula. The interpreted geoelectric data suggest that the IBPT dipped to 15–20 m below the seabed at 350 m offshore. Both results suggest that cold saline water forms beneath grounded ice and floating sea ice in shallow water, causing cryotic benthic temperatures. The freezing point depression produced by salt diffusion can delay or prevent ice formation in the sediment and enhance the IBPT degradation rate. Therefore, salt diffusion may facilitate the release of greenhouse gasses to the atmosphere and considerably affect the design of offshore and coastal infrastructure in subsea permafrost areas.

1. Introduction

Subsea permafrost is defined as seafloor material that remains at or below 0 °C for two or more consecutive years (Van Everdingen, 1998). The thawing of subsea permafrost can destabilize offshore infrastructure (Walker et al., 1983) and release methane to the atmosphere, which may function as a positive feedback to climate warming (e.g., Schuur et al., 2015; Shakhova et al., 2010). Therefore, there are practical engineering and global climate change motivations to investigate subsea permafrost thawing rates. Furthermore, salt transport's effect on permafrost can be explored using the Arctic coast as a natural laboratory. Salt in the sediment porewater lowers the freezing point. Seawater with a salinity of 30.0 (salinity given in Practical Salinity Units) begins to freeze at −1.8 °C (Millero et al., 2008). Therefore, subsea permafrost may contain ice or be ice free, depending on the combined effects of temperature and sediment porewater salinity. Subsea permafrost forms when cold terrestrial permafrost is inundated with seawater, which occurred during deglacial sea level rise after the Last Glacial Maximum (approximately 21,000 years ago) and as a result of gradual permafrost coastline retreat (Romanovskii et al., 2000). Therefore, a large portion of previously nonglaciated and now submerged Arctic shelf regions may be underlain by subsea permafrost, including the Siberian seas, the Bering Sea, and the Alaskan and Canadian Beaufort seas (e.g., Romanovskii & Hubberten, 2001). Once submerged, terrestrial permafrost is no longer exposed to cold mean annual ground surface temperatures, which can be lower than −10 °C along many Arctic coasts. Instead, seawater acts as a thermal buffer between the atmosphere and the sediment, which results in significantly warmer upper boundary conditions that warm the underlying permafrost. If the water depth exceeds the maximum sea ice thickness and the mean annual water temperature is above 0 °C, the permafrost thaws, and a talik begins

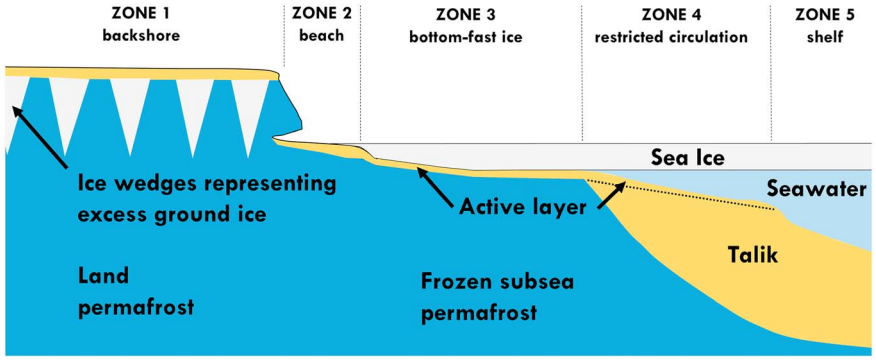

Figure 1. Subsea permafrost zones adapted from Osterkamp (2001).

to form. Even if the mean annual bottom water temperature is below 0 °C, a cryotic talik may still form if sufficient salt transport into the sediment depresses the freezing point. For heavily concentrated brines, the freezing point of water can be as low as −10 °C as shown by perennial springs in the Canadian High Arctic (e.g., Pollard et al., 1999) and even −50 °C for Don Juan Pond in Antarctica (Dickson et al., 2013). Near Arctic coasts, brines may be created in shallow water bodies like lagoons and nearshore zones with rapidly eroding coastlines (e.g., Osterkamp et al., 1989). The thermal and salinity boundary conditions change as inundation time increases, and thus with water depth and distance to shore. As described by Osterkamp (2001), terrestrial permafrost will transition through subaquatic phases defined by occasional submergence, shallow waters with ice grounding, restricted circulation zones with highly saline cryotic benthic conditions in spring, and finally deep water with nearly constant benthic conditions year-round (Figure 1).

To understand subsea permafrost evolution over decadal to millennial timescales, thermal modeling is a suitable approach. One of the first subsea permafrost models to couple heat and salt diffusion was given by Harrison and Osterkamp (1978) for the Alaskan Beaufort Sea. In their models, salt degraded ice-bearing permafrost, but it could not diffuse below the thawed layer. For the Laptev Sea shelf, transient thermal models with dynamic upper boundary conditions have been used to investigate the fate of submerged taliks (Nicolsky & Shakhova, 2010), as well as subsea permafrost evolution for multiple climatic and glacio-eustatic cycles (Romanovskii et al., 1997). In both studies, the freezing curves were shifted for specific salt concentrations, but salt transport was not modeled. Bogorodskii et al. (2018) presented a coupled salt and heat flow model for sea ice growth, brine rejection, and seasonal freezing of surface sediments on the Laptev Sea shelf, but the depth to subsea ice-bearing permafrost was not modeled. Therefore, there is a need for coupled heat and salt diffusion models for subsea permafrost similar to Dmitrenko et al. (2011) as a means to understand its evolution as boundary conditions change with time. Alternative mechanisms of salt transport due to convection or fingering (e.g., Gosink & Baker, 1990; Harrison & Osterkamp, 1978) were not modeled in this paper.

The modeled results of ice-bearing permafrost depths versus inundation time can be compared to and validated by field observations. For example, offshore boreholes and mean erosion rates derived from historical remote sensing imagery are an effective way to calculate ice-bearing permafrost degradation rates (Osterkamp & Harrison, 1982; Rachold et al., 2007; Shakhova et al., 2017). If boreholes are not available, geoelectric methods have proven to be effective at mapping the depth to ice-bearing subsea permafrost (e.g., Overduin et al., 2016, 2012; Sellmann et al., 1989) and the depth to permafrost below freshwater thermokarst lakes (e.g., You et al., 2017). The electrical resistivity tomography method is effective at delineating unfrozen and frozen sediment, because there is an increase in electrical resistivity as water freezes and forms ice (Kneisel et al., 2008). However, this increase in resistivity is mainly due to the decrease in unfrozen water content. Therefore, the resistivity of subaquatic permafrost soils is highly dependent on porosity, grain size, temperature, and the quantity of total dissolved solids in the porewater. As a result, the transition from relatively low to high resistivity could be sharp or gradual depending on the physical and chemical conditions of subaquatic sediments. For example, laboratory studies by Overduin et al. (2012) and Kang and Lee (2015) showed that the resistivity of frozen silty sands can range from below 10 Ω·m to over 1,000 Ω·m, depending on the temperature and porewater salinity. Alternative geophysical methods like ground-penetrating radar have proven to be effective at mapping taliks below freshwater grounded ice zones (Stevens et al., 2009) but

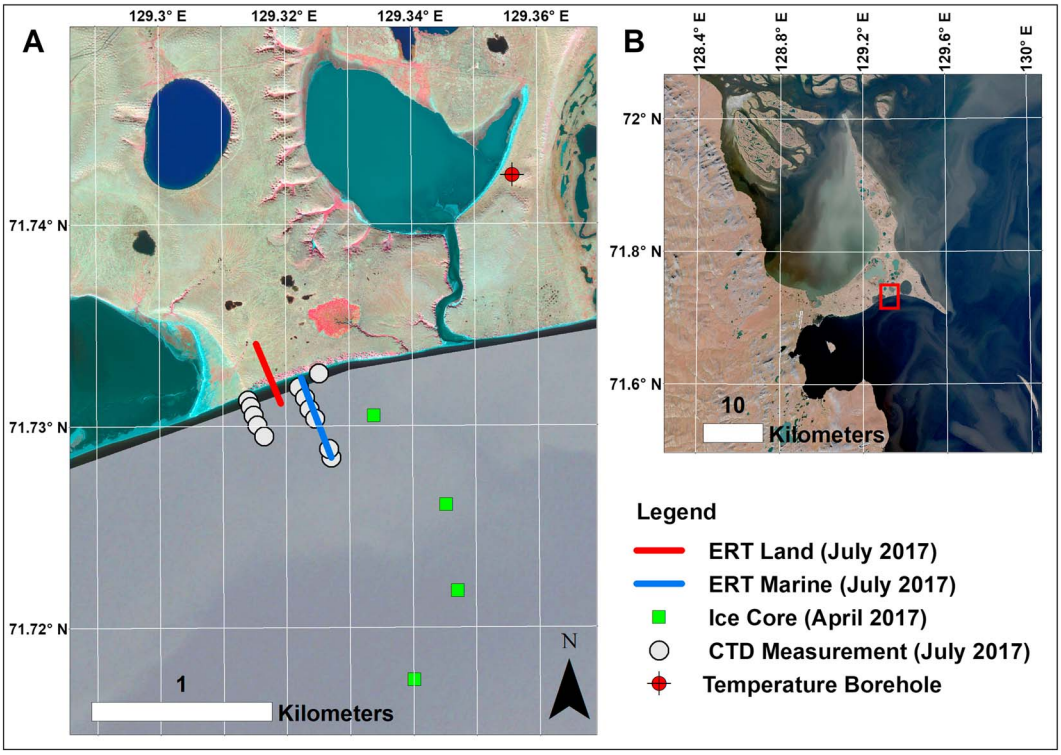

Figure 2. (a) High-resolution satellite image (30-cm ground resolution WorldView-3 image from 2 September 2016) of the southern coastline of the Bykovsky Peninsula and the main study site; (b) The Bykovsky Peninsula's position east of the Kharaulakh Ridge. ERT = electrical resistivity tomography; CTD = conductivity, temperature, and depth.

are not suited for highly electrically conductive saltwater (Annan, 2004). While passive seismic has been recently used to map the depth to ice-bearing subsea permafrost (Overduin et al., 2015a), it is a technique still in development and not practical to achieve the desired spatial resolution of this study. Active seismic methods have been used to map the depth to deep ice-bearing subsea permafrost offshore in the Laptev Sea (Hinz et al., 1998) but are less effective techniques in shallow coastal waters and are not sensitive to subtle changes of salt in the porewater of frozen sediment. Therefore, the electrical resistivity tomography method was considered the most appropriate for subsea permafrost mapping.

The overarching goal of this paper is to demonstrate how changing boundary conditions during inundation of terrestrial permafrost affect its distribution, temperature, and composition below the sea. We coupled a salt diffusion model to the existing CryoGRID2 heat conduction model (Westermann et al., 2013) to numerically predict the evolution of subsea permafrost offshore of the Bykovsky Peninsula in the Laptev Sea. The model's upper boundary conditions were constrained by field data from expeditions in April 2017 and July/August 2017, data from previous work reported in the literature, boreholes, and remote sensing. The modeled outputs were compared to the ice-bearing permafrost degradation rates estimated from geoelectric surveys perpendicular to shore and coastal erosion rates derived from satellite data.

2. Study Area

2.1. Geology

The Bykovsky Peninsula is located southeast of the Lena Delta in the western part of the Buor-Khaya Gulf of the Laptev Sea in northeastern Siberia, Russia (Figure 2). Cape Muostakh, the southeastern limit of the peninsula, is located approximately 20 km eastnortheast of Tiksi, a harbor town and the closest urban settlement. The peninsula is an erosional remnant of an accumulation plain that started to form in the Late Pleistocene in the foreland of the Kharaulakh Ridge (Grosse et al., 2007). The erosion of the Kharaulakh Ridge through nival and seasonal hydrological processes was the main sediment supply for the accumulation of medium to fine-grained ice-rich deposits known as the Yedoma Ice Complex. During the late stage of the Sartan (Weichselian) glacial, increased meltwater from perennial snow patches and higher precipitation

rates resulted in higher erosion rates of the Kharaulakh Ridge's valley deposits, which ultimately disconnected the accumulation plain from its sediment source. In the late Glacial and early Holocene, a warming and wetting climate resulted in intense thermokarst development. In line with global deglaciation, marine transgression in the Laptev Sea (Bauch et al., 2001), and ingression into low-lying areas such as thermokarst lakes and basins, as well as mechanical and thermal erosional processes, produced the landscape of the Bykovsky Peninsula seen today (Romanovskii et al., 2000). The Yedoma Ice Complex ranges from the top of the peninsula's highlands (up to 45 m above sea level) to 15 m below sea level (Grosse et al., 2007; Grigoriev, 1993). The total ice content (wedge ice and intrasedimentary ice) of the Yedoma Ice Complex can reach 87% by volume (Günther et al., 2015). Sediments within the Yedoma Ice Complex at or below sea level range from silty fine-grained sand to medium sand (Grosse et al., 2007; Schirrmeister et al., 2002). Beneath the Yedoma Ice Complex, the sediments range from silty sand to sand and may contain massive cryostructures with pore ice (Grosse et al., 2007). Below the aforementioned sediments lies coarse-grained sandy gravel. The depth to the top of coarse-grained sandy gravel was reported to be 9 m below sea level on the Western Bykovsky Peninsula and down to 29 m below sea level on the Eastern Bykovsky Peninsula.

2.2. Subsea Permafrost and Coastal Erosion

Offshore of the Bykovsky Peninsula, the lower part of the Yedoma Ice Complex is submerged and is thus undergoing subsea permafrost thawing. The thickness of subsea permafrost on the Laptev Sea shelf can be hundreds of meters thick (Romanovskii et al., 1997), and its presence may extend up to 350 km offshore (Soloviev, 1981). Offshore of Muostakh Island, repeated borehole measurements separated by 31–32 years indicated an ice-bearing subsea permafrost degradation rate of 0.14 m/year (Shakhova et al., 2017). Furthermore, geoelectric observations offshore of Muostakh Island showed that the degradation rate of ice-bearing subsea permafrost decreased from 0.4 m/year immediately after inundation to 0.1 m/year 60–110 years after submergence from coastal erosion (Overduin et al., 2016). The same study also demonstrated that the depth to ice-bearing subsea permafrost at a given distance perpendicular to shore is inversely correlated with the coastal erosion rate. On the Bykovsky Peninsula, the coastal erosion rate is related to the orientation of the shoreline (Lantuit et al., 2011). From 1951 to 2006, the mean erosion rate was as high as 1.05 m/year for north-facing shores and as low as 0.42 and 0.27 m/year for south and southeast-facing shorelines, respectively.

2.3. Marine Environmental Conditions

The southern shoreline of the Bykovsky Peninsula lies in Tiksi Bay, which is a marine environment affected by the outflow of the Lena River. Due to its isolation behind Muostakh Island and Cape Muostakh, sea ice tends to be preserved longer than in the Central Laptev Sea (Günther et al., 2015). Northeast of Muostakh Island in 7.2 m water depth, Overduin et al. (2016) recorded hourly benthic temperature and electrical conductivity data from 01.09.2008 to 31.08.2009. The mean annual seabed temperature was 0.5 °C, but seabed temperatures reached values lower than −1 °C below the ice in winter and spring. The mean annual electrical conductivity of the water was 7,100 μS/cm, but values were as high as 15,000 μS/cm underneath the ice in winter. Following ice breakup, the influence of the Lena River discharge resulted in an electrical conductivity less than 300 μS/cm. The sea ice season in Tiksi Bay and the Buor-Khaya Gulf typically starts in late September/early October and ends in June. The mean annual air temperature in Tiksi between 1932 and 2016 was −12.8 °C (World Meteorological Organization station in Tiksi), and the average day for which air temperatures started to dip below 0 °C was 20 September.

2.4. Study Site Rationale

We chose to investigate subsea permafrost offshore of the Bykovsky Peninsula because of the availability of previously published data sets for offshore seawater temperature and salinity, coastal erosion rates, undisturbed permafrost temperatures, and cryostratigraphy to assist the CryoGRID2 model setup. The land to marine transect shown in Figure 2 was carried out at this specific location along the shoreline because it intersected undisturbed permafrost free of drained thermokarst lake basins. Therefore, based on terrestrial borehole and instrumentation data, the initial permafrost temperature prior to inundation could be reasonably estimated.

3. Fieldwork

3.1. Seawater and Ice Properties

As part of a drilling expedition for lagoons and freshwater lakes in April 2017, four ice cores were drilled on a survey line perpendicular to Bykovsky's southern coast (Figure 2). The ice and snow thickness ranged

from 1.3 to 1.5 m and 0.1 to 0.3 m, respectively. Hence, the average ice thickness was 1.4 m, and the average snow thickness was 0.2 m. In July 2017, seawater properties were measured using a Sontek^{TM} CastAway conductivity, temperature, and depth (CTD) sensor with a built-in GPS. The maximum offshore water temperature during the field campaign was 7 °C. With regards to conductivity, the CTD showed values as low as 770 μS/cm (0.6 PSU) on 20 July 2017 for the offshore geoelectric transect. By 29 July 2017, the electrical conductivity increased to almost 1,000 μS/cm (0.8 PSU). The freshening effect of the Lena River decreases and the electrical conductivity of the offshore water increases toward the onset of sea ice formation. The Soil Moisture and Ocean Salinity sensor is from a polar orbiting satellite, providing high temporal resolution data at high latitudes with a spatial resolution of 30–50 km. An average of six pixels from the Soil Moisture and Ocean Salinity sensor east of the Lena Delta show that the practical salinity of seawater increased from 1.7 on 17 August 2017 to 8.5 on 29 September 2017. Therefore, in the models, the initial salinity was assumed to be 8.5 PSU at the onset of ice formation. Charkin et al. (2017) showed that the subice winter salinity of two oceanographic stations just southeast of Bykovsky Peninsula's Cape Muostakh varied from 8.5 to 12.4 PSU for the 2011–2015 period. In addition, the summer salinity at Cape Muostakh was 0.8 PSU (Charkin et al., 2017). The water conductivity the day of the marine resistivity survey was 730 μS/cm and showed very minimal variation with depth. When converted to electrical resistivity, the result was 13.7 Ω·m.

3.2. Geoelectric Surveys and Bathymetry

An IRIS^{TM} Syscal Pro Deep Marine system was used for the marine survey. The 120 m geoelectric cable with floating electrodes was towed behind a small inflatable boat, and the device was equipped with a GPS and an echo sounder to record the position and water depth at the boat locations. The cable had an electrode separation of 10 m, two current electrodes, and eleven potential electrodes. The only array type used for the subaquatic survey was the Reciprocal Wenner-Schlumberger array. Apparent resistivity measurements were taken every 5 m of trip distance. The marine survey presented in this paper started with the boat 140 m perpendicular to shore and the first potential electrode 10 m perpendicular to shore. The geoelectric survey ended with the boat 440 m perpendicular to shore and last potential electrode 430 m from shore. Bathymetry was collected until a distance of 510 m offshore. The survey line is shown is Figure 2. The terrestrial and submerged electrodes survey was performed with a Skala^{TM} electrical survey system. The survey line consisted of several semilines in a roll-along pattern with partial overlap. The electrode separation was 5 m and the survey line is shown is Figure 2.

3.3. Electrical Resistivity Inversions

The apparent resistivity data were inverted with RES2DINV^{TM} software. The apparent resistivity data for terrestrial, submerged (i.e., on the seabed), and floating electrodes were combined into one data set. Although there was a lateral offset between the terrestrial and marine surveys, the subsurface was assumed to have similar properties since they are both perpendicular to the part of the coastline defined by undisturbed Yedoma permafrost. However, floating electrodes that overlapped submerged electrodes were removed to avoid having two electrodes at the same location with different elevations. From the shoreline to 110 m offshore where we had submerged electrodes, we defined a water layer of limited extent with a resistivity of 13.7 Ω·m. From 110 m offshore to the end of the survey line, we had floating electrodes. Robust data constraints were used and the vertical to horizontal flatness filter ratio was set to 0.25. After seven iterations, the absolute error between modeled and observed resistivity was 3.8%.

4. CryoGRID2 Model Setup Coupled With Salt Diffusion

CryoGrid2 is a one-dimensional heat transfer model used to simulate the transient evolution of ground temperatures, with focus on soil freezing processes (Westermann et al., 2013, 2017). In this paper, we add diffusion of salt and its interaction with ground freezing to the existing model framework, which effectively leads to a coupling between the partial differential equations for heat and mass (salt) transfer. While diffusion of heat and salt are independent of each other for unfrozen ground, freezing/thawing is determined by both heat transfer and the freezing point of the porewater given by its salinity. To derive the governing equations for ground temperature T (°C) and porewater salinity c (mol/m^3) expressed as the molar concentration of all ions, we start with the one-dimensional continuity equations for internal energy E (J/m^3) and total salt concentration C (mol/m^3) within a unit volume. C is connected to the porewater salinity through

the unfrozen volumetric water content θ_w as $C = c\theta_w$.

$$\frac{\partial E}{\partial t} + \frac{\partial}{\partial z} F_{\text{heat}} = 0, \tag{1}$$

$$\frac{\partial C}{\partial t} + \frac{\partial}{\partial z} F_{\text{salt}} = 0. \tag{2}$$

Hereby, t (s) denotes time, z the vertical coordinate (m), and F_{heat} and F_{salt} the diffusive fluxes of heat and salt given by

$$F_{\text{heat}} = -\kappa_h \frac{\partial T}{\partial z},$$

$$F_{\text{salt}} = -d_s \frac{\partial c}{\partial z},$$

where κ_h (W/mK) is the thermal conductivity and d_s (m^2/s) the salt diffusivity. The salt diffusivity is derived from the salt diffusion coefficient (d_{s0} [m^2/s]), unfrozen volumetric water content (θ_w), and tortuosity (τ) as $d_s = d_{s0}\theta_w/\tau$. These fluxes can be obtained from the spatial derivatives of the two state variables of the coupled system, T and c.

To obtain equation (1) in dependency of T and c, we expand the time derivatives in terms of the partial derivatives of T and c, using an intermediate step over the water content $\theta_w(T, c)$ to separate the effects of sensible heat (first term) and latent heat (second and third terms).

$$\frac{\partial E}{\partial t} = \frac{\partial E}{\partial T}\frac{\partial T}{\partial t} + \frac{\partial E}{\partial \theta_w}\frac{\partial \theta_w}{\partial T}\frac{\partial T}{\partial t} + \frac{\partial E}{\partial \theta_w}\frac{\partial \theta_w}{\partial c}\frac{\partial c}{\partial t}, \tag{3}$$

$$\frac{\partial C}{\partial t} = \frac{\partial C}{\partial c}\frac{\partial c}{\partial t} + \frac{\partial C}{\partial \theta_w}\frac{\partial \theta_w}{\partial T}\frac{\partial T}{\partial t} + \frac{\partial C}{\partial \theta_w}\frac{\partial \theta_w}{\partial c}\frac{\partial c}{\partial t}. \tag{4}$$

$\partial E/\partial T = c_h$ is the volumetric heat capacity, while $\partial E/\partial \theta_w = L_f$ is connected to the volumetric latent heat of fusion of water, $L_f = 334$ MJ/m^3. Furthermore, differentiating the relationship $C = c\theta_w$ leads to $\partial C/\partial c = \theta_w$ and $\partial C/\partial \theta_w = c$. Rearranging equations (1), (2), (3), and (4) yields a coupled system of differential equations:

$$\left(c_h + L_f \frac{\partial \theta_w}{\partial T}\right)\frac{\partial T}{\partial t} + L_f \frac{\partial \theta_w}{\partial c}\frac{\partial c}{\partial t} - \frac{\partial}{\partial z}\left(\kappa_h \frac{\partial T}{\partial z}\right) = 0, \tag{5}$$

$$c\frac{\partial \theta_w}{\partial T}\frac{\partial T}{\partial t} + \left(\theta_w + c\frac{\partial \theta_w}{\partial c}\right)\frac{\partial c}{\partial t} - \frac{\partial}{\partial z}\left(d_s \frac{\partial c}{\partial z}\right) = 0. \tag{6}$$

To numerically solve equations (5) and (6), we first apply the method of lines (Schiesser, 1991) to discretize the spatial derivatives of T and c (i.e., the last term in equations (5) and (6)) as finite differences, yielding an ordinary differential equation system in terms of time derivatives of T and c. The system can be decoupled using standard linear algebra, resulting in two independent ordinary differential equations for $\partial T/\partial t$ and $\partial c/\partial t$, which are solved with the MATLAB ode45 solver (Hindmarsh et al., 2005).

For this purpose, the derivatives of the water content with respect to temperature and porewater salinity, $\partial \theta_w/\partial T$ (the "freezing characteristic curve" of the material) and $\partial \theta_w/\partial c$, must be evaluated in each time step. We employ the freezing characteristic of Dall'Amico et al. (2011) and shift the onset of freezing according to Millero et al. (2008) to represent the depression of the freezing point in the brine.

Table 1
Subsea Permafrost Evolution Simulations

Scenario	Salt diffusion into sediment	Initial seawater salinity (PSU) prior to ice formation
A	Yes	8.5
B	No	8.5
C	Yes	30
D	No	30

4.1. Simulations

All simulations were run with a 5-day time step. The total length of each simulation was 1,400 years, because this was enough time to compare modeled subsea permafrost evolution to ice-bearing subsea permafrost degradation rates interpreted from marine geoelectric data if we assumed a coastal erosion rate of 0.25 m/year (Lantuit et al., 2011). In this paper, four simulation results are presented (Table 1). Scenarios A and B simulated subsea permafrost evolution under the brackish water conditions observed at the Bykovsky Peninsula with and without salt diffusion into the sediment, respectively. For scenarios A and B, the mean annual benthic temperature was 0.5 °C for a 4.6 m water depth (maximum water depth in model run) following measurements from Overduin et al. (2016), who found that the mean annual benthic temperature was 0.5 °C offshore of Muostakh Island in 7.2 m water depth. The maximum water depth of 4.6 m was the mean water depth measured by the echo sounder 140–510 m from shore. The minimum and maximum water depths along this survey line were 4.0 and 5.1 m, respectively. Scenarios C and D simulated subsea permafrost evolution under typical Arctic seawater conditions without a terrestrial freshwater influence with and without salt diffusion into the sediment, respectively. For scenarios C and D, the mean annual benthic temperature was −0.7°C for a 4.6 m water depth.

4.2. Surface Forcing and Boundary Conditions

As subsea permafrost evolves, it will transition through the different zones described by Osterkamp (2001). Therefore, the upper boundary conditions change as water deepens and depend on whether or not ice grounding occurs. The bathymetric survey perpendicular to the coastline and an erosion rate were used to determine the water depth for each year of the model simulation (Figure 3). For the first year of inundation, the water depth was assumed to be 0.5 m. The upper boundary conditions for temperature and seawater salt concentration were calculated prior to running the model. Each model year began on 20 September, because this was the average day (1932–2016) when air temperatures dipped below 0 °C in the fall. For air temperature, daily means for the 1932–2016 period were calculated using data from the Tiksi World Meteorological Organization station. The upper boundary conditions transitioned through different phases throughout a model simulation year as described below. Daily boundary condition function examples are shown in Figure 4 to demonstrate the relationship between benthic temperature and salinity.

4.2.1. Sea Ice Formation Period

During this period, the upper boundary conditions were applied at the water/seabed interface. The benthic temperature was equal to the freezing point of water, which was a function of the seawater salt concentra-

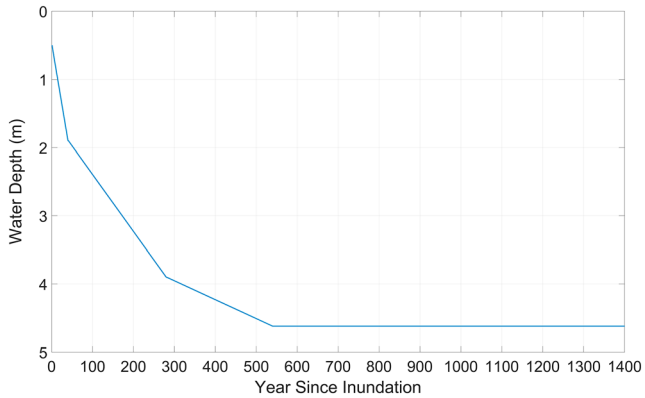

Figure 3. Bathymetry as a function of time assuming an erosion rate of 0.25 m per year.

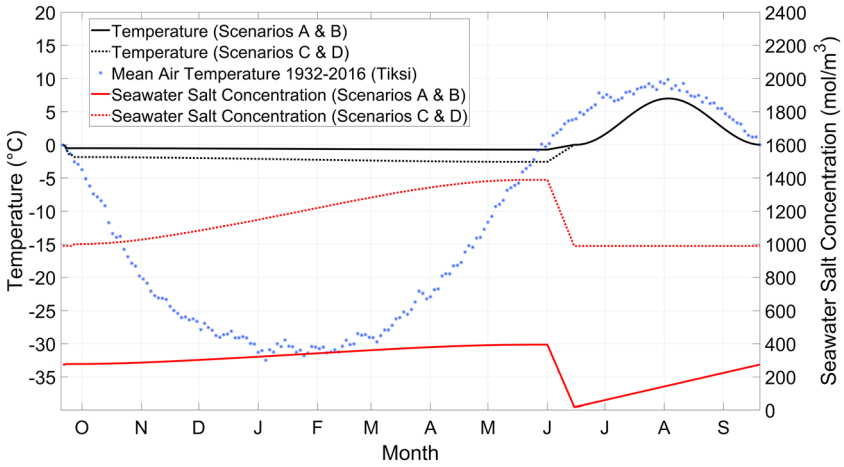

Figure 4. Daily upper boundary conditions for year 1,400 for scenarios A to D. This graph shows the relationship between benthic temperature and salinity for the Bykovsky Peninsula and typical Arctic seawater scenarios.

tion. The seawater salt concentration was a function of the initial concentration prior to sea ice formation and sea ice thickness. The sea ice thickness was driven by air temperature, snow thickness, and seawater salt concentration, which increased as ice thickness increased. It was assumed that all salt was rejected into the underlying water when ice formed so that the freezing point of the remaining brine, T_f, decreased dynamically during ice formation. This model ignored any underlying water circulation that would have kept the seawater salt concentration and thus the freezing point of water constant during ice formation. The snow thickness was assigned a constant value of 0.2 m for every day until ice breakup. The equation for sea ice thickness is shown in equation (7), where d_{ice} (m) = ice thickness, d_{snow} (m) = snow thickness, t (s) is time, T_{air} (°C) is air temperature, T_f (°C) is the freezing point of water, L_f is the volumetric latent heat of fusion, and κ (W/mK) is a weighted thermal conductivity of a two-layer system consisting of snow and ice (equation (8)). This is identical to the sea ice growth modeling equations for a two-layer snow-ice system presented by Leppäranta (1993).

$$\frac{\partial d_{\text{ice}}}{\partial t} = -\kappa \frac{T_{air}(t) - T_f(t)}{\left(d_{\text{ice}}(t) + d_{\text{snow}}(t)\right) L_f}, \tag{7}$$

$$\kappa_{(d_{\text{snow}}+d_{\text{ice}})} = \kappa_{\text{ice}}\kappa_{\text{snow}} \frac{d_{\text{ice}} + d_{\text{snow}}}{\kappa_{\text{ice}} d_{\text{snow}} + \kappa_{\text{snow}} d_{\text{ice}}}. \tag{8}$$

The sea ice thickness increased until T_{air} was greater than T_f, at which point the sea ice thickness was stable. Similar to the 2017 field data, the maximum modeled sea ice thickness was 1.4 m for floating sea ice.

4.2.2. Ice Grounding Phase

If ice grounding occurred, grid cells were added for snow and ice. Therefore, the upper boundary conditions were applied at the air/snow interface. The temperature was equal to the air temperature, and the salt concentration was equal to zero. The initial temperature within the snow and ice layers was determined by linearly interpolating between the air and seabed temperatures on the first day of ice grounding. In addition, the initial salt concentration within the snow and ice layers was zero. Due to cold snow and ice temperatures and very low unfrozen water content, any upward diffusion of salt from the seabed was negligible.

4.2.3. Open Water Season

The ice broke up when T_{air} went above 0 °C for two consecutive days. In a nongrounded ice case, T_f increased linearly for 15 days until it was equal to 0 °C, and the seawater salt concentration decreased linearly for 15 days until a minimum of 0.6 PSU for scenarios A and B and 30 PSU for scenarios C and D. The minimum salt concentration for scenarios A and B was equal to the minimum CTD measurement and the 15-day period is consistent with typical ice breakup periods for thermokarst lakes in the Lena Delta (Boike et al., 2015). For an ice grounding case, the benthic temperature was held at 0 °C, and the seawater salt concentration was held at 0.6 PSU for 15 days for scenarios A and B and 30 PSU for scenarios C and D. Following the ice breakup period, the water temperature increased as a sine function until a peak value of 7 °C in midsummer.

Table 2
Thermal Properties of the Minerals, Water, Ice, and Snow

Material	Thermal conductivity (W/mK)	Volumetric heat capacity (MJ/m^{3}K)
Mineral	5.72	2.0
Water	0.57	4.2
Ice	2.20	1.9
Snow	0.31	0.57

This is the maximum water temperature measured with the CTD in July 2017. The water temperature then decreased as a sine function to 0 °C on 20 September. After ice breakup, the seawater salt concentration increased linearly until the initial seawater salt concentration of 8.5 PSU on 20 September for scenarios A and B. For scenarios C and D, the seawater salt concentration was held constant at 30 PSU.

4.3. Dynamic Model Grid

The size of the first grid cell at the water/seabed interface was 0.1 m and increased as a log space function with 499 cells until a depth of 6 km below the seabed. This was the model mesh for the sea ice formation and open water seasons. If ice grounding occurred, the final temperature and porewater salinity regimes just prior to ice grounding were used as an initial condition for the grid cells below the seabed for the next time step. Grid cells 0.05 m thick were added for the snow and ice layers during the ice grounding phase. Once ice breakup occurred, the grid cells for snow and ice were removed. For the next time step, the final temperature and porewater salinity regimes on the last day of ice grounding were used as an initial condition for grid cells below the seabed for the next time step in the open water season.

4.4. Material Properties

Based on the stratigraphic work of Grosse et al. (2007) and Schirrmeister et al. (2002), the sediment type was assumed to be a sand. In terms of mineralogy, Nolting et al. (1996) showed that the sediments in the Laptev Sea and Lena Delta were predominantly siliceous (approximately 60%). Therefore, 60% of the soil's mineral fraction was assumed to be quartz, and 40% other mineral solids. The quartz was assigned a mineral thermal conductivity of 8.8 W/mK, and other minerals a thermal conductivity of 3.0 W/mK (Williams & Smith, 1991). The mineral thermal conductivity was calculated from equation (9) (Andersland & Ladanyi, 2004), where κ_s is the mineral thermal conductivity, κ_q is the thermal conductivity of quartz, κ_o is the thermal conductivity of other mineral solids, and q is the quartz fraction of the mineral soil.

$$\kappa_s = {\kappa_q}^q {\kappa_o}^{(1-q)} \tag{9}$$

As in Westermann et al. (2013), the net thermal conductivity is dependent on the mineral thermal conductivity, as well as the ice and unfrozen water fractions. In this model, the ice and unfrozen water fractions were a function of porosity, temperature, and porewater salinity. The mineral, unfrozen water, and ice fractions also determined the volumetric heat capacity of the sediment. Organic fractions were not included in this model and the sediment was assumed to be saturated. The thermal properties are summarized in Table 2. Since the applied version of CryoGRID2 did not include subsidence from melting excess ground ice, the maximum porosity at the seabed was set to 0.5, which phenomenologically accounted for ice-rich material. The porosity decreased with depth according to Lee (2005) to account for the increasing compaction of sediments. The parameters of the freezing characteristic curves for sand were defined by Dall'Amico et al. (2011). In Dall'Amico et al. (2011), the curves shown are for fresh sediments with no salts. The inclusion of salt in CryoGRID2 shifts the freezing characteristic curves as salt lowers the freezing point of water. For salt transport, the salt diffusion coefficient (d_{s0}) was equal to 0.8e–9 m^2/s and the sediment tortuosity (τ) was equal to 1.5.

4.5. Initial Conditions

The initial ground thermal regime was set using a steady state function with a ground surface temperature of −10 °C, a geothermal heat flux of 50 mW/m^2, and zero salinity everywhere in the model domain. The mean ground temperature was based on the permafrost temperature at the depth of zero annual amplitude in a Yedoma hill borehole west of Ivashkina Lagoon (Schirrmeister et al., 2018). Therefore, the modeled initial permafrost thickness was 819 m, which is consistent with the 650 to 1,000 m range summarized by Nicolsky and Shakhova (2010) for the Tiksi Bay area.

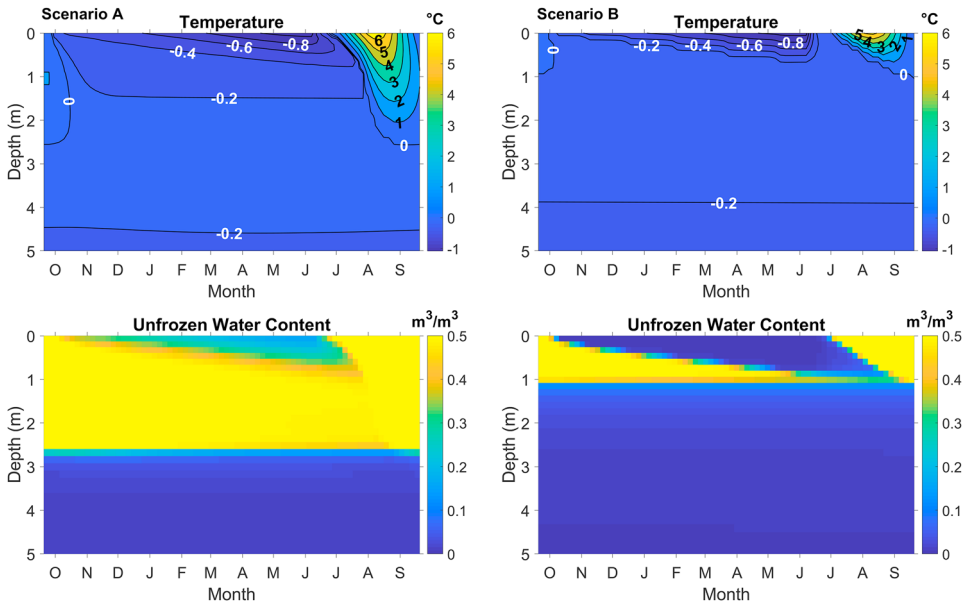

Figure 5. This figure compares the seasonal changes of shallow sediments for scenario A (Bykovsky Peninsula with salt diffusion) and scenario B (Bykovsky Peninsula without salt diffusion). The results are shown for year 110 after inundation, which is when a sediment cell maintained 0% ice content all year after submergence for scenario A.

5. Results

5.1. Heat and Salt Diffusion Modeling

5.1.1. Seasonal Impacts of Salt Diffusion on Subsea Permafrost

The impact of salt diffusion on permafrost processes for the Bykovsky Peninsula is clearly demonstrated in Figure 5. Here temperature and unfrozen water content outputs are presented for year 110 for scenarios A and B. Year 110 was chosen because it is the first year when a sediment cell maintained 0% ice content all year after submergence for scenario A. For scenario B without salt diffusion, the seabed started to freeze completely in early October. By early June, the frozen active layer merged with the ice-bearing permafrost. In early July following ice breakup, the active layer started to thaw and reached a maximum depth of 1 m by late September. For scenario A with salt diffusion, the seabed only partially froze during the year. For example, at the beginning of June, the unfrozen water content was 0.15 at the seabed and 0.30 at a depth of 0.6 m. In early July following ice breakup, the partially frozen layer began to thaw and was completely gone by early August. The depth to ice-bearing permafrost for year 110 was approximately 2.7 m. For scenario A, the summer temperature wave propagated to more than twice the depth of scenario B. Over the long term, this seasonal damping of heat flow by latent heat had a considerable impact of modeled ice-bearing permafrost degradation rates. For scenario C with salt diffusion, similar seasonal processes occurred. In early June in year 110, the unfrozen water content was 0.25 at the seabed despite a seabed temperature of −3.8 °C. Therefore, there was little ice to melt during the open water season. For scenario D without salt diffusion, no talik formed because the mean annual seabed temperature was negative, and salt could not diffuse into the sediment to lower the freezing point. Therefore, an active layer of 0.9 m refroze completely by early January.

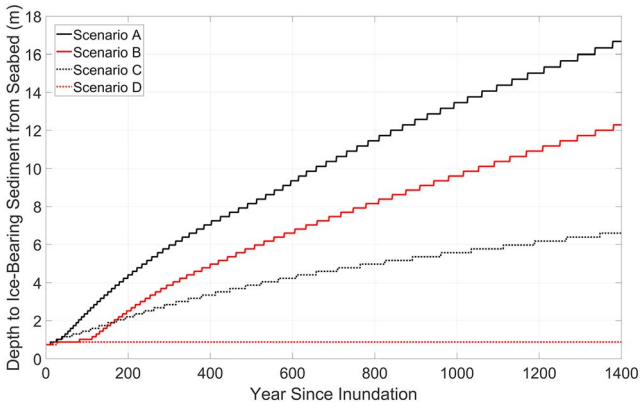

Figure 6. Depth to ice-bearing sediment in late September as a function of inundation time (0.25 m/year erosion rate) for the Bykovsky Peninsula (scenarios A and B) and typical Arctic seawater (scenarios C and D). Scenarios A and C include salt diffusion into the sediment, and scenarios B and D do not. Since the results are shown for the end of September, the depth to ice-bearing sediment did not start at 0 m for the first year after inundation. In the early years following inundation, the depth to ice-bearing sediment represents the active layer depth and not the talik depth.

5.1.2. Long-Term Subsea Permafrost Evolution for the Bykovsky Peninsula (Model Scenarios A and B)

The depth to ice-bearing sediment at the end of September as a function of inundation time (0.25 m/year erosion rate) for the model runs is presented in Figure 6. All depths are reported from the water/seabed interface. For scenario A, the depth to ice-bearing sediment ranged from 0.7 to 0.9 m for the first 25 years of the simulation. In fact, this was

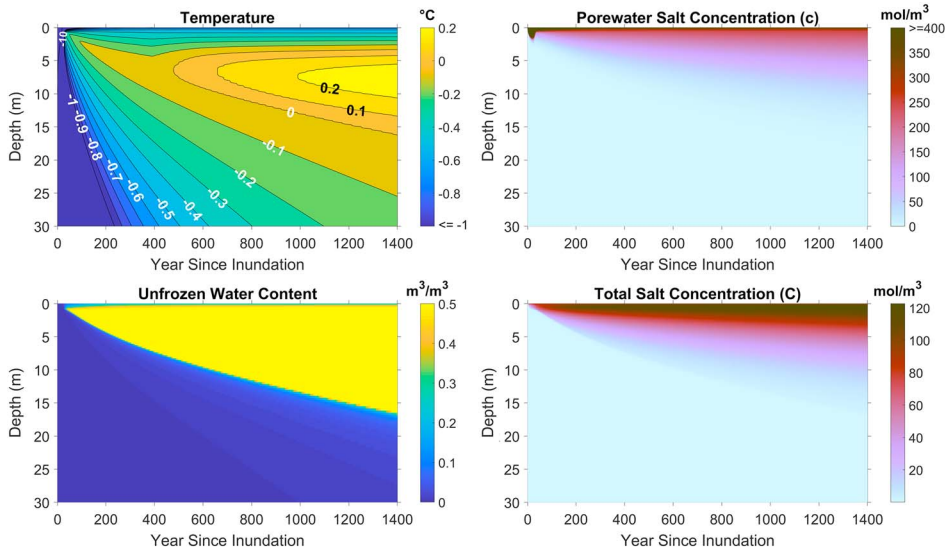

Figure 7. The evolution of temperature, unfrozen water content, porewater salinity, and total salt concentration as a function of inundation time for scenario A (Bykovsky Peninsula with salt diffusion). For visual clarity, the yearly outputs at the end of April are presented.

the duration of the ice grounding period. At the halfway point of the simulation (year 700), the depth to ice-bearing permafrost was 10.4 m and at the end of the simulation (year 1,400), it was 16.7 m. If the 4.6 m water depth is included, this corresponds to a mean ice-bearing permafrost degradation rate of 0.015 m/year. For scenario B, the depth to ice-bearing sediment remained at or below 1.3 m for the first 130 years. By year 130, the water depth was already 2.6 m and not subject to ice grounding. A sediment cell with perennially ice-free conditions did not develop until year 135 at a depth of 1.2 m. At the halfway point of the simulation (year 700), the depth to ice-bearing permafrost was 7.7 m, and at the end of the simulation (year 1,400), it was 12.3 m. If the 4.6 m water depth is included, this corresponds to a mean ice-bearing permafrost degradation rate of 0.012 m/year.

For scenario A with salt diffusion, four graphics of temperature, unfrozen water content, porewater salt concentration, and total salt concentration versus inundation time are shown in Figure 7. For clarity, only the yearly outputs at the end of April are shown. Once again, depths are from the water/seabed interface. By year 1,400, the permafrost was warm below the base of the talik and had a temperature warmer than −0.1 °C 20 m below the seabed. Over the course of the simulation, the total salt concentration increased and diffused to greater depths, but the diffusion rate slowed with inundation time. However, the porewater salinity showed a different trend. In the first few decades of the simulation when ice grounding and highly saline water were a factor, the porewater salinities were higher than 400 mol/m^3. However, they were concentrated in exceptionally low amounts of unfrozen water. Therefore, the total salt concentrations in the grid cells were low and did not result in significant thawing during this period. The maximum porewater salinity in the near-surface sediment prior to freezing was 240 mol/m^3, which corresponds to a freezing point of −0.5 °C, and this mitigated seasonal freezing of the seabed.

5.1.3. Long-Term Subsea Permafrost Evolution for Typical Arctic Seawater (Model Scenarios C and D)

For typical Arctic seawater with no coastal freshwater influence, the long-term subsea evolution trends are quite different compared to the Bykovsky Peninsula. For scenario C with salt diffusion, the depth to ice-bearing permafrost was 4.6 m at the halfway point of the simulation (year 700) and 6.6 m at the end of the simulation (year 1,400). If the 4.6 m water depth is included, this corresponds to a mean ice-bearing permafrost degradation rate of 0.008 m/year. For scenario D without salt diffusion, the depth to ice-bearing sediment was 0.7 m for the first 30 years of the simulation but then stabilized at 0.9 m for the rest of the model run. Therefore, there was no ice-bearing permafrost degradation for scenario D.

For scenario C with salt diffusion, four graphics of temperature, unfrozen water content, porewater salt concentration, and total salt concentration versus inundation time are shown in Figure 8. Once again, only the yearly outputs at the end of April are shown, and the depths are from the water/seabed interface. Similar to

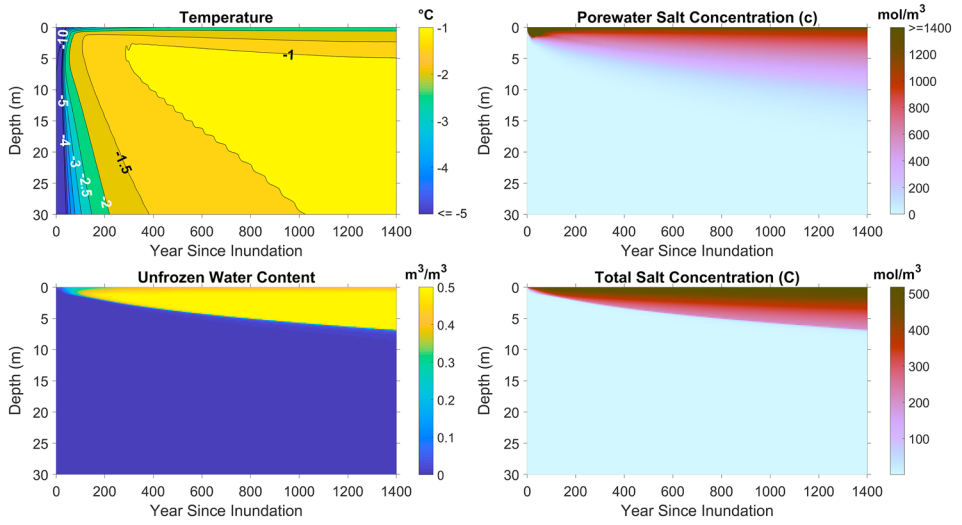

Figure 8. The evolution of temperature, unfrozen water content, porewater salinity, and total salt concentration as a function of inundation time for scenario C (typical Arctic seawater with salt diffusion). For visual clarity, the yearly outputs at the end of April are presented.

Figure 7, the porewater salt concentrations were high during the first few decades of the simulation (>1,400 mol/m^3). However, the sediment remained frozen as shown by the very low unfrozen water content. By year 1,400, the talik remained cryotic with temperatures ranging from −1.8 °C just below the seabed to −0.8 °C at the ice-bearing permafrost table. After 1,400 years of inundation, the temperature within the ice-bearing permafrost shown in Figure 8 was between −0.7 °C (the mean annual benthic temperature) and −0.9 °C. Most importantly, the depth of the cryotic talik was directly correlated to the depth of salt penetration as illustrated by the unfrozen water content and total salt concentration.

5.2. Electrical Resistivity

The inverted results combining floating electrodes, submerged electrodes, and terrestrial electrodes are shown in Figure 9. At the shoreline, resistivity transitioned from high (10^3 Ω·m) to low (10^2 Ω·m) from onshore to offshore, respectively. Offshore, there was an increase in resistivity with increasing depth, from 10^1 Ω·m at the seafloor to 10^2 Ω·m 30 m below sea level. Offshore resistivity increased most sharply with depth between the 16 and 128 Ω·m contours. However, there was an anomaly 120 m perpendicular to shore where the 16 to 128 Ω·m contours slightly increased to shallower depths. Below the 128 Ω·m contour, the resistivity ranged from 128 to 512 Ω·m, except for the very nearshore zone (<20 m from the coast). The resis-

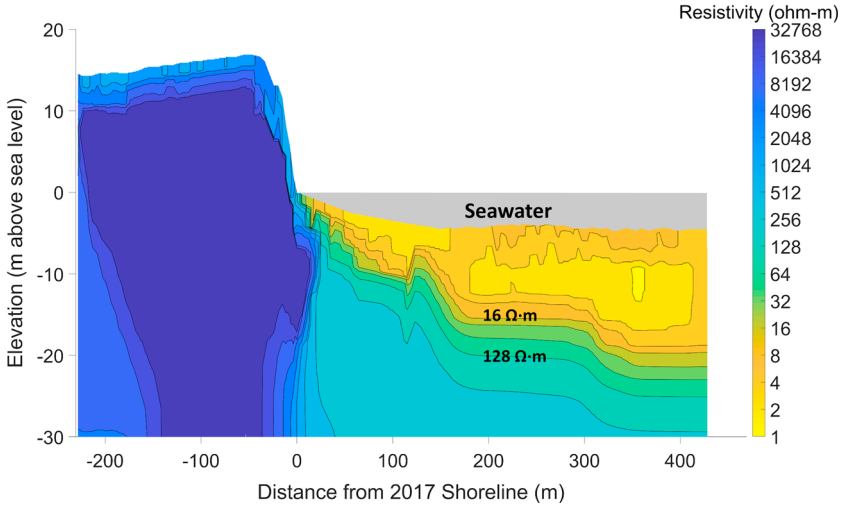

Figure 9. The inverted resistivity results for the land and offshore data. The maximum resistivity in the scale bar is capped at 32,768 Ω·m.

tivity above the 16 Ω·m contour offshore predominantly ranged from 2 to 8 Ω·m. On land, the resistivity exceeded 30,000 Ω·m, but resistivity values this high were also observed below the seabed within 20 m of the coast. On land, resistivity increased from 4,000 Ω·m at the surface to over 30,000 Ω·m a few meters below the ground surface.

6. Discussion

6.1. Heat and Salt Diffusion Modeling

6.1.1. Simulation Results

The seasonal freezing of the seabed has a major impact on the modeled long-term ice-bearing permafrost table degradation rates. As shown in Figure 5, the shallow seabed does not completely freeze in the winter and spring when salt diffuses into the sediment. Instead, a slushy mixture of water and ice is present. Consequently, less energy is required to melt ice in summer, which permits greater warming of the underlying sediment compared to the scenario without salt diffusion. Over the course of 1,400 years, the depth to ice-bearing permafrost is 16.7 m with salt diffusion compared to only 12.3 m without salt diffusion. Essentially, the combination of subzero temperatures and salt behaves similarly to warm noncryotic boundary conditions. The seasonal freezing of the seabed is also modeled by Bogorodskii et al. (2018) for various water depths in the Tiksi Gulf. Their modeled seasonal freezing depths are mostly less than ours, possibly because they use a lower thermal conductivity for the sediment. Therefore, future work should consider the impacts of sediment type on seasonal freezing of the seabed.

In addition, the bathymetry has a considerable impact on subsea permafrost thawing. For scenario A, the depth to ice-bearing sediment at the end of September does not exceed 0.9 m for the first 25 years of the simulation (Figure 6). This is because the first 25 years of inundation have sufficiently shallow water depths to produce grounded ice. Although the benthic salinity can reach concentrations over 2,000 mol/m^3 prior to ice grounding, rapid cooling from atmosphere-seabed coupling completely freezes the shallow seabed when bedfast ice occurs. As reported by Burn (2005), lake-bottom thermal temperatures can be as low as −20 °C for shallow grounded ice zones. Therefore, rapid cooling from atmosphere-seabed coupling dominates over highly concentrated brine conditions at the seabed in winter and spring for the Bykovsky Peninsula. For scenario B, the depth to ice-bearing sediment in late September remains at or below 1.3 m for the first 130 years of inundation (Figure 6) because salt does not diffuse into the sediment to lower the freezing point. As a result, the seabed active layer completely refreezes every year. Even without ice grounding conditions (after year 25), cold saline water below the ice in winter and spring freezes the seabed and shallow sediment.

For typical Arctic seawater with negative mean annual benthic temperatures, the development of a talik is entirely dependent on salt diffusion. As illustrated by scenario D (Figure 6), the depth of ice-bearing permafrost increases from 0.7 m to 0.9 m for the first 30 years but then remains stable at 0.9 m for the rest of the simulation. This is essentially an increase in the active layer thickness since permafrost warms as it transitions from land to sea. Despite warming permafrost temperatures, a talik cannot develop if salt does not penetrate the sediment to lower the freezing point. If salt diffusion is included (scenario C), the talik growth rate is entirely driven by how fast salt diffuses into the sediment. This is different from model scenario A (Bykovsky Peninsula) where the mean annual benthic temperature is positive. For scenario A, salt is not a prerequisite for talik formation but instead acts to exacerbate talik growth by minimizing seasonal freezing of the seabed and shallow sediments.

The modeling work by Harrison and Osterkamp (1978) clearly shows that salt diffusion degrades subsea permafrost when the mean freezing point of water at the seabed is lower than the negative mean annual seabed temperature. However, salt diffusion models were insufficient to explain the rapid rate of subsea permafrost degradation observed at Prudhoe Bay. Therefore, convective processes in coarse-grained sediments with a high hydraulic conductivity were suggested as a means to explain the subsea permafrost degradation rates at Prudhoe Bay. In our scenarios A and C, the inclusion of convective processes would result in more saline and vertical profiles of porewater salinity above the subsea permafrost table. These salt regimes could minimize seasonal freezing of the seabed even more and enhance molecular diffusion at the talik/ice-bearing permafrost boundary for scenarios A and C by increasing the porewater salt concentration gradient. Both processes would increase the subsea permafrost degradation rate.

6.1.2. Model Limitations

Groundwater flow, which is not included in our model, could cause convective heat transfer and exacerbate permafrost warming rates (e.g., de Grandpré et al., 2012). With regards to salt transport, there is considerably

more work to be done. For salt diffusion, sensitivity analyses on the salt diffusion coefficient and sediment tortuosity should be carried out. The sediment tortuosity, in particular the connectivity of unfrozen water films, is heavily affected by ground ice structure (Fortier et al., 1994). Perhaps more importantly, there are additional salt transport mechanisms like convection that are not modeled. In coarse-grained sediments, bulk fluid flow can enhance salt transport rates, which may result in faster rates of subsea permafrost thawing (e.g., Harrison & Osterkamp, 1978). One of the model's major limitations is its inability to melt excess ice and subside the seafloor. Therefore, the Yedoma Ice Complex is not included in these simulations. Future development should consider a dynamically changing bathymetry that adjusts itself to excess ice melt, like the CryoGRID3 model for thermokarst lakes (Westermann et al., 2016). Our model also simplifies sea ice growth dynamics, because there is no snow ramp-up function and the temperature of the snow or ice surface is assumed to be equal to air temperature. For our study area, we considered the surface temperature approximation reasonable, because Langer et al. (2011a) and Langer et al. (2011b) showed that the difference between seasonal air and snow surface temperature averages was always less than 1 °C at a site in the Lena River Delta from 2007 to 2009. However, in other areas, such as Svalbard, the difference between air and snow surface temperatures can be quite large (Westermann et al., 2009). Future models could be greatly improved by incorporating approximations for snow surface temperature based on standard temperature and humidity data (Raleigh et al., 2013).

6.2. Geoelectric Surveys

Figure 9 shows resistivity decreasing with increasing distance offshore for any sediment depth. Since we do not know the resistivity as a function of temperature, we assume that the transition from unfrozen to frozen sediment occurs within the range of 16 to 128 Ω·m based on previous work (section 1). Since the permafrost underlying the talik is likely warm near the interface, the electrical transition to frozen material could be gradual due to subtle changes in unfrozen water content and salt (Overduin et al., 2012). We acknowledge that the positions of the resistivity contours may be sensitive to the selected inversion parameters. Therefore, the goal of the resistivity surveys was to determine an order of magnitude estimate for the subsea permafrost degradation rate using a published rate of mean coastal retreat.

The resistivity contour spikes 120 m offshore are interpreted to be an anomaly, as this is the transition zone between the submerged and floating electrodes in the inversion. Generally, the survey shows 16–128 Ω·m contours that decrease in slope with increasing distance offshore. This fits the expected trend of decreasing ice-bearing permafrost degradation rates versus inundation time (Osterkamp, 2001). The transition from 16 to 128 Ω·m also becomes less steep with increasing distance offshore, because subsurface temperatures and salinity vary more gradually with depth after long periods of inundation. However, the decreasing steepness of the 16–128 Ω·m transition with increasing distance offshore could be partially due to decreasing resolution with depth as well. Based on the geoelectric data, the maximum ice-bearing permafrost table depth 350 m offshore is interpreted to be between 15 and 20 m from the seabed. The subsea permafrost resistivities above 30,000 Ω·m within 20 m of the coast could be due to cold benthic temperatures in shallow waters where ice grounding occurs. Beyond 20 m offshore where ice grounding likely does not occur (water depth exceeds 2 m), subsea permafrost resistivity decreases to values between 128 and 512 Ω·m. Given the resistivity values of ice-bearing subsea permafrost, we speculate that it is warm and may contain more unfrozen water. Therefore, it could be a mixture of sand and silt, since the unfrozen water content of pure sand decreases quite rapidly below 0 °C (Anderson et al., 1973). The subsea ice-bearing permafrost porewater may also contain some salts as demonstrated by borehole observations offshore of Muostakh Island (Overduin et al., 2016), and these salts could result in lower resistivity values for frozen material (Overduin et al., 2012).

6.3. Subsea Permafrost Degradation Rates

Both the geoelectric data and heat and salt flow modeling were used to assess permafrost degradation rates on the Bykovsky Peninsula. Clearly, scenario A with salt diffusion fits the geoelectric data assuming a mean coastal erosion rate of 0.25 m/year as shown in Figure 10. However, as shown by Lantuit et al. (2011), the coastal erosion rates can be nearly 0.50 m/year for south facing shorelines. If this is the case, then the heat and salt flow models generally underestimate the ice-bearing permafrost degradation rates. Warmer benthic temperatures than assumed would account for such an underestimation. In the models, the maximum water temperature is 7 °C, because it matched the fieldwork data and generated identical mean annual benthic conditions to those observed offshore of Muostakh Island (Overduin et al., 2016). However, the thermokarst lakes and saltwater lagoons showed temperatures as high as 10 °C in July 2017, and Overduin et al. (2016) also showed that offshore benthic temperatures could exceed 10 °C in summer. Another possibility is the

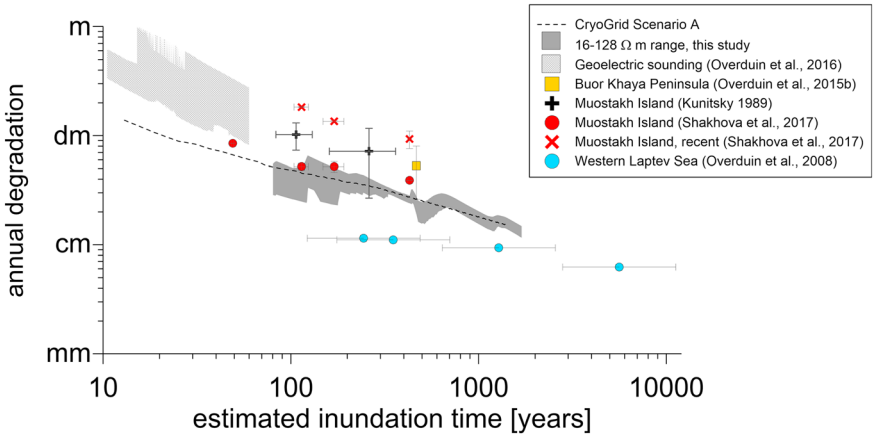

Figure 10. Subsea permafrost degradation rates derived from the CryoGRID2 model results with salt diffusion for the Bykovsky Peninsula (scenario A), and the geoelectric results are compared to published subsea permafrost degradation rates in Siberia. The studies include long-term (i.e., since inundation) and recent degradation rates from borehole work at Muostakh Island (Shakhova et al., 2017; Kunitsky, 1989), as well as degradation rates derived from a borehole at the Buor-Khaya Peninsula (Overduin et al., 2015b), several boreholes in the Western Laptev Sea (Overduin et al., 2008), and geoelectric results offshore of Muostakh Island (Overduin et al., 2016).

inaccurate representation of ice volumes. If the base of ice-rich permafrost is shallow and the volumetric ice content of subsea sediment is closer to 30% (a typical value for sand), then the modeled ice-bearing permafrost degradation rates would be faster due to the reduced latent heat required to melt ice in the sediment. Alternatively, the inclusion of the Yedoma Ice Complex in the model would likely result in substantially slower ice-bearing permafrost degradation rates in the simulations as the ice melts. In addition to ice content, the porewater salinity of permafrost upon inundation has a major impact on talik development as shown by Nicolsky and Shakhova (2010), who demonstrated that thermokarst underlain by saline permafrost in the East Siberian Arctic Shelf could result in open taliks after only approximately 5,000 to 7,500 years of inundation in areas of relative high geothermal heat fluxes. Therefore, salt-contaminated ground prior to inundation could result in faster rates of subsea permafrost degradation. The geothermal heat flux is particularly important for thawing the base of subsea permafrost. This has also been demonstrated by the modeling work of Romanovskii et al. (1997), who showed that ice-bonded permafrost in the middle part of the Laptev Sea Shelf (45 to 80 m isobaths) thaws completely in areas with high geothermal heat fluxes. Therefore, sensitivity analyses for the geothermal heat flux should be performed for models with simulation times spanning complete marine transgressions.

The Lena River also has a considerable impact on subsea permafrost evolution, primarily because warm freshwater discharge generates mean coastal benthic temperatures above 0 °C. The Lena River's influence on seawater salinity also controls benthic temperatures. A lower initial seawater salinity in September may lead to warmer benthic temperatures under the ice cover, but also thicker sea ice. Therefore, in shallow coastal waters, freshwater could lead to a longer period of ice grounding upon inundation and delayed talik formation. Thicker sea ice generated from a thinner snow cover and colder air temperatures could lead to an extended period of ice grounding as well. If seawater circulation is neglected, thicker ice generated from colder climates or less snow could also result in more saline and colder subice water temperatures and slower subsea permafrost degradation rates. Our study is site specific, so the modeled sea ice conditions were calibrated to field data. However, Bogorodskii et al. (2018) showed that the maximum sea ice thickness was 2 m in the Tiksi Gulf south of the Bykovsky Peninsula in 2014–2015. Sea ice dynamics should be modeled to accommodate diverse boundary conditions for large scale models of subsea permafrost.

The mean annual subsea permafrost degradation rates are calculated from sea level and not the seabed. For the geoelectric data, the mean ice-bearing permafrost degradation rate ranged from 0.014 to 0.018 m/year for a 0.25 m/year erosion rate. For model scenario A, which best represented the conditions at the Bykovsky Peninsula, the mean ice-bearing permafrost degradation was 0.015 m/year. Figure 10 compares the scenario A model results and the geoelectric data to published subsea permafrost degradation rates for Siberia. The results from this study fit within the same order of magnitude as the long-term mean degradation rates of 0.014 m/year reported by Rachold et al. (2007) for the Western Laptev Sea. However, Overduin et al. (2008)

updated the erosion rates for the Western Laptev Sea work and found that the mean annual degradation rate was less than 0.01 m/year after 1,400 years of inundation. The model and geoelectric results fit very well with the long-term mean annual subsea permafrost degradation rates (i.e., since inundation) calculated by Shakhova et al. (2017) for Muostakh Island but can be up to an order of magnitude less than the recent mean annual degradation rates calculated from repeated borehole observations. The results of this study are also up to 1 order of magnitude less than the degradation rates reported by Overduin et al. (2016) offshore of Muostakh Island for the first 100 years of inundation. In general, the ice-bearing permafrost degradation rates are slower for the Western Laptev Sea compared to Muostakh Island (Kunitsky, 1989; Overduin et al., 2016; Shakhova et al., 2017), Buor-Khaya Peninsula (Overduin et al., 2015b), and the Bykovsky Peninsula (Figure 10). This could be because the Western Laptev Sea has negative mean annual benthic temperatures, as it is less affected by warm and fresh river runoff (Rachold et al., 2007). This finding fits with the model results, which showed that the degradation rate for scenario A (Bykovsky Peninsula) was more than twice as fast as scenario C (typical Arctic seawater). However, studies from northern Alaska show faster ice-bearing permafrost degradation rates in areas with mean negative benthic temperatures. For example, at Prudhoe Bay, the mean annual ice-bearing permafrost table degradation rate was 0.03 m/year after 1,000 years of inundation, and it has been suggested that salt transport from convection plays a major role in the coarse-grained sediments (e.g., Harrison & Osterkamp, 1978; Osterkamp et al., 1989). Therefore, a logical next step for coupled heat and salt flow modeling is the inclusion of bulk fluid flow dynamics for assessing the impact of salt transport on subsea permafrost.

7. Conclusions

The coupled salt and heat transport in the version of the CryoGrid2 model presented here addresses a knowledge gap in our current understanding of the relative roles of thermal and chemical thawing of submarine permafrost. In this paper, the modeled subsea ice-bearing permafrost table degradation rates were compared with observed ice-bearing permafrost degradation rates inferred from geoelectric data and remotely sensed coastal erosion rates on the Bykovsky Peninsula in Siberia. Salt diffusion lowers the freezing point of water and therefore minimizes seasonal freezing of the seabed. Therefore, less energy is used to melt ice in summer, which over time, results in deeper depths to ice-bearing permafrost. Hence, cold subzero benthic temperatures combined with salt behaves similarly to warm positive benthic temperatures without salt. The models also show that rapid cooling from atmosphere-seabed coupling in grounded ice zones dominates over heavily concentrated brines in shallow waters to delay talik formation. The geoelectric data suggests that the top of ice-bearing permafrost was 15-20 m below the seabed 350 m offshore, which is consistent with the model results with salt diffusion. The geoelectric data shows that the mean ice-bearing permafrost degradation rates are consistent with multiple borehole studies in the region. Predictive modeling and field observations of subsea permafrost are important, as it is the degradation of the permafrost table that will be critical to infrastructure, to shallow shelf processes, and the release of any free and dissolved gas trapped within the permafrost. Furthermore, a deeper understanding of salty permafrost dynamics is critical for the exploration of active hydrological systems in extreme and cold permafrost environments.

Acknowledgments
The field data presented in this paper are available from the PANGAEA website (https://doi.org/10.1594/PANGAEA.895887). The fieldwork was funded by the PETA-CARB project (ERC 338335), Novosibirsk State University (Grant 5-100), the Russian Foundation for Basic Research (RFBR/RFFI) (Grants 18-05-70091 and 18-45-140057), the Federal Ministry of Education and Research in Germany (Grant 030F0764B), and the Program of Fundamental Scientific Research (FSR) from the IPGG (Grants 0331-2019-0007 and 0331-2019-0016). Logistical support was provided by Hydrobase in Tiksi, the Lena Delta Reserve, and Waldemar Schneider. S. Westermann acknowledges funding by SatPerm (Grant 239918; Research Council of Norway) and PermaNor (Grant 255331/E10; Research Council of Norway). We are also very thankful to Bennet Juhls (Freie Universität Berlin), who was part of the summer expedition and provided Soil Moisture and Ocean Salinity (SMOS) data. Lastly, we are indebted to George Maximov (Melnikov Permafrost Institute (MPI), Yakutsk, Russia), who provided invaluable scientific input and technical help during the expedition.

References

Andersland, O. B., & Ladanyi, B. (2004). *Frozen ground engineering*. Hoboken, NJ: John Wiley.

Anderson, D. M., Tice, A. R., & McKim, H. L. (1973). The unfrozen water and the apparent specific heat capacity of frozen soils. In *Second International Conference on Permafrost, Yakutsk, USSR. North American contribution* (pp. 289–295).

Annan, A. (2004). Ground-penetrating radar. In D. J. Daniels (Ed.), *Near-surface geophysics* (pp. 357–438). Mississauga, Ontario, Canada: Society of Exploration Geophysicists.

Bauch, H. A., Kassens, H., Naidina, O. D., Kunz-Pirrung, M., & Thiede, J. (2001). Composition and flux of holocene sediments on the eastern laptev sea shelf, arctic siberia. *Quaternary Research*, *55*(3), 344–351.

Bogorodskii, P. V., Pnyushkov, A. V., & Kustov, V. Y. (2018). Seasonal freezing of a subwater ground layer at the laptev sea shelf. In M. G. Velarde, R. Yu. Tarakanov, & A. V. Marchenko (Eds.), *The Ocean in Motion, Springer Oceanography* (Vol. 4, pp. 611–625). Cham, Switzerland: Springer.

Boike, J., Georgi, C., Kirilin, G., Muster, S., Abramova, K., Fedorova, I., et al. (2015). Thermal processes of thermokarst lakes in the continuous permafrost zone of Northern Siberia-observations and modeling (Lena River Delta, Siberia). *Biogeosciences*, *12*(20), 5941.

Burn, C. R. (2005). Lake-bottom thermal regimes, Western Arctic Coast, Canada. *Permafrost and Periglacial Processes*, *16*(4), 355–367.

Charkin, A. N., Van Der Loeff, M. R., Shakhova, N. E., Gustafsson, Ö., Dudarev, O. V., Cherepnev, M. S., et al. (2017). Discovery and characterization of submarine groundwater discharge in the siberian arctic seas: A case study in the buor-khaya gulf, laptev sea. *The Cryosphere*, *11*(5), 2305.

Dall'Amico, M., Endrizzi, S., Gruber, S., & Rigon, R. (2011). A robust and energy-conserving model of freezing variably-saturated soil. *The Cryosphere*, *5*(2), 469.

de Grandpré, I., Fortier, D., & Stephani, E. (2012). Degradation of permafrost beneath a road embankment enhanced by heat advected in groundwater. *Canadian Journal of Earth Sciences*, *49*(8), 953–962.

Dickson, J. L., Head, J. W., Levy, J. S., & Marchant, D. R. (2013). Don Juan Pond, Antarctica: Near-surface CaCl 2-brine feeding Earth's most saline lake and implications for Mars. *Scientific Reports*, *3*, 1166.

Dmitrenko, I. A., Kirillov, S. A., Tremblay, L. B., Kassens, H., Anisimov, O. A., Lavrov, S. A., et al. (2011). Recent changes in shelf hydrography in the Siberian Arctic: Potential for subsea permafrost instability. *Journal of Geophysical Research*, *116*, C10027. https://doi.org/10.1029/2011JC007218

Fortier, R., Allard, M., & Seguin, M.-K. (1994). Effect of physical properties of frozen ground on electrical resistivity logging. *Cold Regions Science and Technology*, *22*(4), 361–384.

Gosink, J., & Baker, G. (1990). Salt fingering in subsea permafrost: Some stability and energy considerations. *Journal of Geophysical Research*, *95*(C6), 9575–9583.

Grigoriev, M. (1993). Cryomorphogenesis of the Lena Delta mouth area, Permafrost Institute, Academy of Science USSR, Siberian Department. Yakutsk (pp. 1–176).

Grosse, G., Schirrmeister, L., Siegert, C., Kunitsky, V. V., Slagoda, E. A., Andreev, A. A., & Dereviagyn, A. Y. (2007). Geological and geomorphological evolution of a sedimentary periglacial landscape in northeast siberia during the late quaternary. *Geomorphology*, *86*(1), 25–51.

Günther, F., Overduin, P. P., Yakshina, I. A., Opel, T., Baranskaya, A. V., & Grigoriev, M. N. (2015). Observing Muostakh disappear: Permafrost thaw subsidence and erosion of a ground-ice-rich island in response to Arctic summer warming and sea ice reduction. *The Cryosphere*, *9*(1), 151–178.

Harrison, W., & Osterkamp, T. E. (1978). Heat and mass transport processes in subsea permafrost 1. An analysis of molecular diffusion and its consequences. *Journal of Geophysical Research*, *83*(C9), 4707–4712.

Hindmarsh, A. C., Brown, P. N., Grant, K. E., Lee, S. L., Serban, R., Shumaker, D. E., & Woodward, C. S. (2005). Sundials: Suite of nonlinear and differential/algebraic equation solvers. *ACM Transactions on Mathematical Software (TOMS)*, *31*(3), 363–396.

Hinz, K., Delisle, G., & Block, M. (1998). Seismic evidence for the depth extent of permafrost in shelf sediments of the Laptev Sea, Russian Arctic. In *Proceedings of the 7th international conference on permafrost* (pp. 453–458).

Kang, M., & Lee, J. (2015). Evaluation of the freezing-thawing effect in sand-silt mixtures using elastic waves and electrical resistivity. *Cold Regions Science and Technology*, *113*, 1–11.

Kneisel, C., Hauck, C., Fortier, R., & Moorman, B. (2008). Advances in geophysical methods for permafrost investigations. *Permafrost and Periglacial Processes*, *19*(2), 157–178.

Kunitsky, V. (1989). *Cryolithology of the lower Lena area*. Yakutsk: Melnikov Institute Press.

Langer, M., Westermann, S., Pattern, S., Piel, K., & Boike, J. (2011a). The surface energy balance of a polygonal tundra site in northern Siberia part 1: Spring to fall. *The Cryosphere*, *5*, 151–171.

Langer, M., Westermann, S., Pattern, S., Piel, K., & Boike, J. (2011b). The surface energy balance of a polygonal tundra site in northern Siberia part 2: Winter. *The Cryosphere*, *5*, 509–524.

Lantuit, H., Atkinson, D., Paul Overduin, P., Grigoriev, M., Rachold, V., Grosse, G., & Hubberten, H.-W. (2011). Coastal erosion dynamics on the permafrost-dominated Bykovsky Peninsula, North Siberia, 1951–2006. *Polar Research*, *30*(1), 7341.

Lee, M. W. (2005). Well log analysis to assist the interpretation of 3-D seismic data at Milne Point. North Slope of Alaska, Tech. rep.

Leppäranta, M. (1993). A review of analytical models of sea-ice growth. *Atmosphere-Ocean*, *31*(1), 123–138.

Millero, F. J., Feistel, R., Wright, D. G., & McDougall, T. J. (2008). The composition of standard seawater and the definition of the reference-composition salinity scale. *Deep Sea Research Part I: Oceanographic Research Papers*, *55*(1), 50–72.

Nicolsky, D., & Shakhova, N. (2010). Modeling sub-sea permafrost in the East Siberian Arctic Shelf: the Dmitry Laptev Strait. *Environmental Research Letters*, *5*(1), 15006.

Nolting, R. F., van Dalen, M., & Helder, W. (1996). Distribution of trace and major elements in sediment and pore waters of the Lena Delta and Laptev Sea. *Marine Chemistry*, *53*(3-4), 285–299.

Osterkamp, T. (2001). Subsea permafrost. In J. H. Steele et al. (Eds.), *Encyclopedia of Ocean Sciences* (pp. 2902–2912). New York: Elservier.

Osterkamp, T., Baker, G., Harrison, W., & Matava, T. (1989). Characteristics of the active layer and shallow subsea permafrost. *Journal of Geophysical Research*, *94*(C11), 16,227–16,236.

Osterkamp, T., & Harrison, W. (1982). Temperature measurements in subsea permafrost off the coast of Alaska. In *4th Canadian Permafrost Conference* (pp. 238–248).

Overduin, P. P., Haberland, C., Ryberg, T., Kneier, F., Jacobi, T., Grigoriev, M., & Ohrnberger, M. (2015a). Submarine permafrost depth from ambient seismic noise. *Geophysical Research Letters*, *42*, 7581–7588. https://doi.org/10.1002/2015GL065409

Overduin, P. P., Liebner, S., Knoblauch, C., Günther, F., Wetterich, S., Schirrmeister, L., et al. (2015b). Methane oxidation following submarine permafrost degradation: Measurements from a Central Laptev Sea shelf borehole. *Journal of Geophysical Research: Biogeosciences*, *120*, 965–978. https://doi.org/10.1002/2014JG002862

Overduin, P. P., Rachold, V., & Grigoriev, M. (2008). The state of subsea permafrost in the western Laptev nearshore zone. In D. L. Kane & K. M. Hinkel (Eds.), *Proceedings of the Ninth International Conference on Permafrost* (Vol. 1, pp. 345–350). Fairbanks, AK: Inst. of North. Eng., University of Alaska Fairbanks.

Overduin, P. P., Westermann, S., Yoshikawa, K., Haberlau, T., Romanovsky, V., & Wetterich, S. (2012). Geoelectric observations of the degradation of nearshore submarine permafrost at barrow (alaskan beaufort sea). *Journal of Geophysical Research*, *117*, F02004. https://doi.org/10.1029/2011JF002088

Overduin, P. P., Wetterich, S., Günther, F., Grigoriev, M. N., Grosse, G., Schirrmeister, L., et al. (2016). Coastal dynamics and submarine permafrost in shallow water of the central laptev sea, east siberia. *The Cryosphere*, *10*(4), 1449.

Pollard, W., Omelon, C., Andersen, D., & McKay, C. (1999). Perennial spring occurrence in the expedition fiord area of Western Axel Heiberg Island, Canadian High Arctic. *Canadian Journal of Earth Sciences*, *36*(1), 105–120.

Rachold, V., Bolshiyanov, D. Y., Grigoriev, M. N., Hubberten, H.-W., Junker, R., Kunitsky, V. V., et al. (2007). Nearshore arctic subsea permafrost in transition. *Eos Transactions American Geophysical Union*, *88*(13), 149–150.

Raleigh, M. S., Landry, C. C., Hayashi, M., Quinton, W. L., & Lundquist, J. D. (2013). Approximating snow surface temperature from standard temperature and humidity data: New possibilities for snow model and remote sensing evaluation. *Water Resources Research*, *49*, 8053–8069. https://doi.org/10.1002/2013WR013958

Romanovskii, N., Gavrilov, A., Kholodov, A., Hubberten, H.-W., & Kassens, H. (1997). Reconstruction of paleogeographic conditions on the Laptev Sea Shelf for late Pleistocene-Holocene Glacioeustatic Cycle (in Russian). *Earth Cryosphere*, *1*, 42–49.

Romanovskii, N. N., & Hubberten, H.-W. (2001). Results of permafrost modelling of the lowlands and shelf of the Laptev Sea Region, Russia. *Permafrost and Periglacial Processes*, *12*(2), 191–202.

Romanovskii, N., Hubberten, H.-W., Gavrilov, A., Tumskoy, V., Tipenko, G., Grigoriev, M., & Siegert, C. (2000). Thermokarst and land-ocean interactions, Laptev Sea Region, Russia. *Permafrost and Periglacial Processes*, *11*(2), 137–152.

Schiesser, W. (1991). The numerical method of lines academic, San Diego, CA.

Schirrmeister, L., Grigoriev, M. N., Strauss, J., Grosse, G., Overduin, P. P., Kholodov, A., et al. (2018). Sediment characteristics of a thermokarst lagoon in the Northeastern Siberian Arctic (Ivashkina Lagoon, Bykovsky Peninsula). *Arktos*, *4*(1), 13.

Schirrmeister, L., Siegert, C., Kunitzky, V. V., Grootes, P. M., & Erlenkeuser, H. (2002). Late quaternary ice-rich permafrost sequences as a paleoenvironmental archive for the Laptev Sea Region in Northern Siberia. *International Journal of Earth Sciences*, *91*(1), 154–167.

Schuur, E., McGuire, A. D., Schädel, C., Grosse, G., Harden, J., Hayes, D., et al. (2015). Climate change and the permafrost carbon feedback. *Nature*, *520*(7546), 171–179.

Sellmann, P. V., Delaney, A. J., & Arcone, S. A. (1989). Coastal subsea permafrost and bedrock observations using dc resistivity. Tech. rep., Cold Regions Research and Engineering Laboratory, Hanover, N.H.

Shakhova, N., Semiletov, I., Gustafsson, O., Sergienko, V., Lobkovsky, L., Dudarev, O., et al. (2017). Current rates and mechanisms of subsea permafrost degradation in the East Siberian Arctic Shelf. *Nature Communications*, *8*, 15872.

Shakhova, N., Semiletov, I., Salyuk, A., Yusupov, V., Kosmach, D., & Gustafsson, Ö. (2010). Extensive methane venting to the atmosphere from sediments of the East Siberian Arctic Shelf. *Science*, *327*(5970), 1246–1250.

Soloviev, V. (1981). Predicted distribution of relic submarine frozen zone (East Arctic seas example). In *Cryolithozone of the Arctic Shelf* [inRussian] (pp. 28–38) Permafrost Inst. Siber. Branch Russ. Acad. Sci., Yakutsk, Russia.

Stevens, C. W., Moorman, B. J., Solomon, S. M., & Hugenholtz, C. H. (2009). Mapping subsurface conditions within the near-shore zone of an arctic delta using ground penetrating radar. *Cold Regions Science and Technology*, *56*(1), 30–38.

Van Everdingen, R. O. (1998). Multi-language glossary of permafrost and related ground-ice terms in Chinese, English, French, German, Icelandic, Italian, Norwegian, polish, Romanian, Russian, Spanish and Swedish. International Permafrost Association, Terminology Working Group.

Walker, D., Hayley, D., & Palmer, A. (1983). The influence of subsea permafrost on offshore pipeline design. In *Proceedings of the 4th International Conference on Permafrost, National Academy Press* (pp. 1338–1343).

Westermann, S., Langer, M., Boike, J., Heikenfeld, M., Peter, M., Etzelmüller, B., & Krinner, G. (2016). Simulating the thermal regime and thaw processes of ice-rich permafrost ground with the land-surface model cryogrid 3. *Geoscientific Model Development*, *9*(2), 523.

Westermann, S., Luers, J., Langer, M., Piel, K., & Boike, J. (2009). The annual surface energy budget of a high-arctic permafrost site on Svalbard, Norway. *The Cryosphere*, *3*(2), 245–263.

Westermann, S., Peter, M., Langer, M., Schwamborn, G., Schirrmeister, L., Etzelmüller, B., & Boike, J. (2017). Transient modeling of the ground thermal conditions using satellite data in the Lena River Delta, Siberia. *The Cryosphere*, *11*(3), 1441.

Westermann, S., Schuler, T., Gisnås, K., & Etzelmüller, B. (2013). Transient thermal modeling of permafrost conditions in Southern Norway. *The Cryosphere*, *7*(2), 719.

Williams, P. J., & Smith, M. W. (1991). The frozen Earth.

You, Y., Yu, Q., Pan, X., Wang, X., & Guo, L. (2017). Geophysical imaging of permafrost and talik configuration beneath a Thermokarst Lake. *Permafrost and Periglacial Processes*, *28*(2), 470–476.